



1 **Dipole Pattern of Summer Ozone Pollution in the east of China and Its**  
2 **Connection with Climate Variability**

3 Xiaoqing Ma<sup>1</sup>, Zhicong Yin<sup>123</sup>

4 <sup>1</sup>Key Laboratory of Meteorological Disaster, Ministry of Education / Joint International Research Laboratory of  
5 Climate and Environment Change (ILCEC) / Collaborative Innovation Center on Forecast and Evaluation of  
6 Meteorological Disasters (CIC-FEMD), Nanjing University of Information Science & Technology, Nanjing  
7 210044, China

8 <sup>2</sup>Southern Marine Science and Engineering Guangdong Laboratory (Zhuhai), Zhuhai, China

9 <sup>3</sup>Nansen-Zhu International Research Centre, Institute of Atmospheric Physics, Chinese Academy of Sciences,  
10 Beijing, China

11 **Corresponding author:** Zhicong Yin (yinzhc@nuist.edu.cn)

12 **Address:** No. 219 Ningliu Road, Pukou District, Nanjing University of Information Science & Technology,  
13 Nanjing 210044, China

14 **Tel.:** (+86) 136 5516 1661

15

16 **Abstract.**

17 Surface O<sub>3</sub> pollution has become one of the most severe air pollution problems in China, which makes it of  
18 practical importance to understand O<sub>3</sub> variability. A south-north dipole pattern of summer-mean O<sub>3</sub> concentration  
19 in the east of China (DP-O<sub>3</sub>), which were centered at North China (NC) and the Pearl River Delta (PRD)  
20 respectively, has been identified from the simulation of a global 3-D chemical transport model for the period  
21 1980–2019. Large-scale anticyclonic (cyclonic) and cyclonic (anticyclonic) anomalies over NC and the PRD  
22 resulted in a sharp contrast of meteorological conditions between the above two regions. The enhanced (restrained)  
23 photochemistry and natural emissions of O<sub>3</sub> precursors in NC and restrained (enhanced) O<sub>3</sub> production in the PRD  
24 contributed to the DP-O<sub>3</sub>. Decreased sea ice anomalies near the Franz Josef Land and associated warm sea surface  
25 in May enhanced the Rossby-wave source over northern Europe and West Siberia, which eventually induced an  
26 anomalous Eurasia-like pattern to influence the formation of the DP-O<sub>3</sub>. The thermodynamic signals of the  
27 southern Indian Ocean dipole were stored in the subsurface and influenced spatial pattern of O<sub>3</sub> pollution in the  
28 east of China mainly through the Hadley circulation. The physical mechanisms behind the modulation of the  
29 atmospheric circulations and related DP-O<sub>3</sub> by these two climate anomalies at different latitudes were evidently  
30 verified by large-scale ensemble simulations of the earth system model.

31 **Key words:** ozone pollution; sea ice; Eurasia pattern; sea surface temperature; meridional circulation



## 32 1. Introduction

33 Surface O<sub>3</sub> is an important air pollutant. Exposure to high concentrations of O<sub>3</sub> is detrimental to both human  
34 health and vegetation ecology (Rider and Carlsen, 2019). Since 2013, surface O<sub>3</sub> concentration has increased  
35 over most parts of China, which is largely attributed to changes in anthropogenic emissions (Xu et al. 2018).  
36 However, previous studies have shown that in addition to its trend of change, surface O<sub>3</sub> concentration also  
37 demonstrated large interannual variations with significant regional differences (Zhou et al. 2013; Chen et al. 2019).  
38 Based on analysis of 11 years of observational data over Hong Kong, Zhou et al. (2013) reported that the  
39 interannual variation of O<sub>3</sub> concentration observed during 2000–2010 could reach up to 30% of the annual average  
40 concentration. The O<sub>3</sub> concentration in Beijing also showed evident interannual variation during 2006–2016. For  
41 example, the O<sub>3</sub> concentrations in the summers of 2012–2013 were lower than that in 2011 and 2014 (Chen et al.  
42 2019).

43 High O<sub>3</sub> events are usually associated with meteorological factors (e.g., intense solar radiation, high air  
44 temperature and low humidity) favorable for O<sub>3</sub> formation, which can accelerate photochemical reaction and  
45 weaken the dispersions and depositions (Han et al. 2020). For example, ozone pollution in China in 2017 was  
46 more serious than that in 2016, which was attributed to the large enhancement of nature emissions of ozone  
47 precursors caused by hot and dry climate condition in 2017 (Lu et al. 2019). In the summer of 2013, the Yangtze  
48 River Delta experienced a severe heat wave with more stagnant meteorological conditions. The upper-level  
49 anticyclonic circulation with sink airflows led to abnormally low atmospheric water vapor content above the  
50 Yangtze River Delta and thus less than normal cloud cover, which was conducive to a strong solar radiation  
51 environment and significant increases in surface ozone (Pu et al. 2017). On the interannual to decadal time scale,  
52 anticyclonic anomalies over North China (NC) were critical for O<sub>3</sub> distribution in the summer and remotely linked  
53 with the effects of Eurasia teleconnection (EU) and west Pacific patterns (Yin et al. 2019).

54 The Arctic sea ice (SI) declined rapidly while its variability has been increasing over the past decades, which  
55 significantly affected summer atmospheric circulations over Eurasia (Lin and Li 2018). The preceding Arctic SI  
56 anomalies could aggravate anomalously high air temperature and drought disasters in NC by triggering EU-like  
57 atmospheric responses in summer (Wang and He 2015). Spring SI anomalies in the Barents Sea could prompt the  
58 Silk Road Pattern and resulted in a north-south dipole pattern of summer air temperature anomalies in the east of  
59 China (Li et al. 2021). When greater than normal SI occurred in the Barents Sea, local 500 hPa geopotential height  
60 would decrease and a wave-chain would form, which subsequently induced more precipitation in the south of East  
61 China but less precipitation in the north (Wang and Guo 2004). Sea surface temperature (SST) in the Pacific and



62 Indian oceans also have significant effects on atmospheric circulation over the east of China (Li and Xiao 2021;  
63 Xia et al. 2021). SST anomalies in the South China Sea and the equatorial Eastern Indian Ocean could trigger the  
64 East Asian - Pacific pattern and resulted in a dipole pattern of summer temperature and precipitation in the east  
65 of China, i.e., areas to the north of the Yangtze River became cold and wet, while areas to the south were hot and  
66 dry (Han and Zhang 2009; Li et al. 2018). Tian and Fan (2019) found that winter SST in the southern Indian  
67 Ocean might affect spring-summer SST anomalies near Australia. In summer, the anomalous Hadley circulation  
68 in the western North Pacific played an important role in summer precipitation over the middle and lower reaches  
69 of the Yangtze River.

70 Although great attention in previous studies has been paid to the increase of ozone pollution, little is known  
71 about changes in the spatial pattern of summer-mean O<sub>3</sub> in the east of China. As revealed by Yin and Ma (2020),  
72 the dominant pattern of daily-varying ozone pollution in the east of China showed an interannual variation that  
73 was mainly driven by the large-scale western Pacific subtropical high and the East Asian deep trough. For example,  
74 the frequent movements of the western Pacific subtropical high and the East Asian deep trough both contributed  
75 to the out-of-phase variations in O<sub>3</sub> over North China and the Yangtze River Delta (Zhao and Wang 2017; Yin  
76 and Ma 2020). However, to the best of our knowledge, whether the north-south dipole pattern of the summer mean  
77 O<sub>3</sub> pollution existed in the east of China still remains unclear. In this study, we attempted to explore the dominant  
78 pattern of summertime O<sub>3</sub> in the east of China and associated physical mechanisms behind. Its connections with  
79 preceding climate variability were also examined. The remainder of this paper was organized as follows. The data  
80 and methods are described in Section 2. Section 3 examined the dipole pattern of summertime O<sub>3</sub> in the east of  
81 China and its possible influencing factors. The associated physical mechanisms were studied in Section 4. Major  
82 conclusions and discussion are provided in Section 5.

## 83 2. Datasets and methods

### 84 2.1 Observations and Reanalysis Dataset

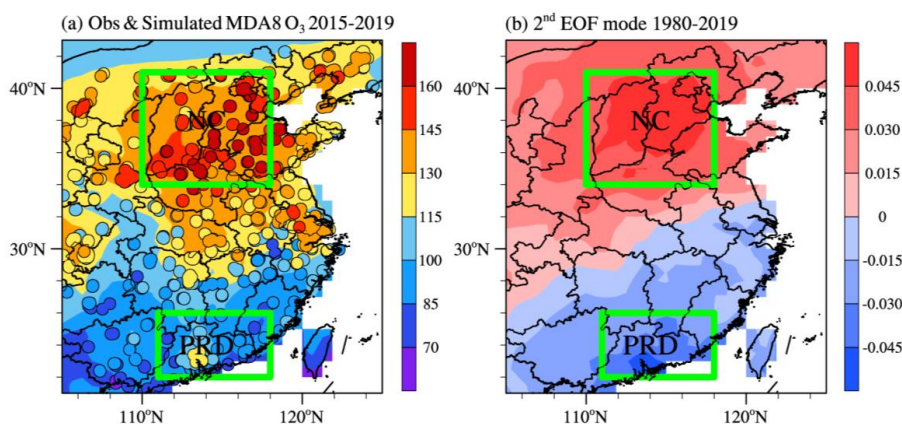
85 Hourly ozone concentration observations from 2015 to 2019 were publicly available at  
86 <https://softnet.net/air/> and the last accessible data were for 23 September 2020. The relevant data were detrended  
87 before all computations were conducted for the study period.

88 Monthly mean meteorological data in global 1° × 1° grids for the period 1980 - 2019 were extracted from  
89 the fifth generation of the European Center for Medium-Range Weather Forecasts reanalysis dataset (Hersbach et  
90 al. 2020), including geopotential height at 500 hPa (Z500), downward solar radiation on the surface (Ssr), low





120 scale from 2015 to 2019 (Yin and Ma 2020). In this study, we first simulated the maximum daily average 8 h  
121 concentration of O<sub>3</sub> (MDA8 O<sub>3</sub>) from 2015 to 2019 and evaluated the performance of GEOS-Chem. Results  
122 indicated that the simulated spatial distribution of MDA8 O<sub>3</sub> was similar to that of observations with a spatial  
123 correlation coefficient of 0.87 (Figure 1a). The observed and simulated summer MDA8 O<sub>3</sub> anomalies in the east  
124 of China also presented consistent interannual differences (Figure S1 a, b). The high consistency in both the  
125 temporal and spatial distributions between the simulations and observations provided a solid evidence to support  
126 the feasibility of the present study.



127  
128 **Figure 1.** (a) Spatial distributions of observed (dots) and GEOS-Chem simulated (shading) summer-mean MDA8 O<sub>3</sub> (unit: μg  
129 m<sup>-3</sup>) for the period 2015–2019. (b) The second EOF spatial pattern of simulated summer-mean MDA8 O<sub>3</sub> from 1980 to 2019.  
130 The simulated O<sub>3</sub> concentrations were produced by GEOS-Chem with fixed emissions but changing meteorological conditions  
131 from 1980 to 2019. The green boxes represent the areas of NC and the PRD.

132 Based the above results, the GEOS-Chem model was then driven by fixed emissions in 2010 and changing  
133 meteorological fields from 1980 to 2019 to highlight the impact of climate variability on O<sub>3</sub> concentration. Results  
134 of this simulation were analyzed to reveal the dominant pattern of ozone pollution in the east of China in summer  
135 and its relationship with preceding climate anomalies.

### 136 2.3 Numerical experiments with CESM-LE

137 To provide evidences that support the proposed connections between SI and SST and large-scale atmospheric  
138 circulations, the simulations of the Community Earth System Model Large Ensemble (CESM-LE) were employed  
139 (Kay et al. 2015). The CESM consists of coupled atmosphere, ocean, land, and sea ice component models. The  
140 40-member ensemble of CESM-LE simulations over the period (1980–2019) includes a historical simulation  
141 (1980–2005) and a representative concentration pathway (RCP) 8.5 forcing simulation (2006–2019). To confirm  
142 the impact of preceding climate variability and associated physical mechanisms, composite analyses were



143 conducted based on the three years with the lowest and highest simulated SI in each member. The composite  
144 results of atmospheric circulations could be considered as the relevant atmospheric responses associated with the  
145 preceding climate variability.

### 146 3. Dipole pattern of summer O<sub>3</sub> and possible influencing factors

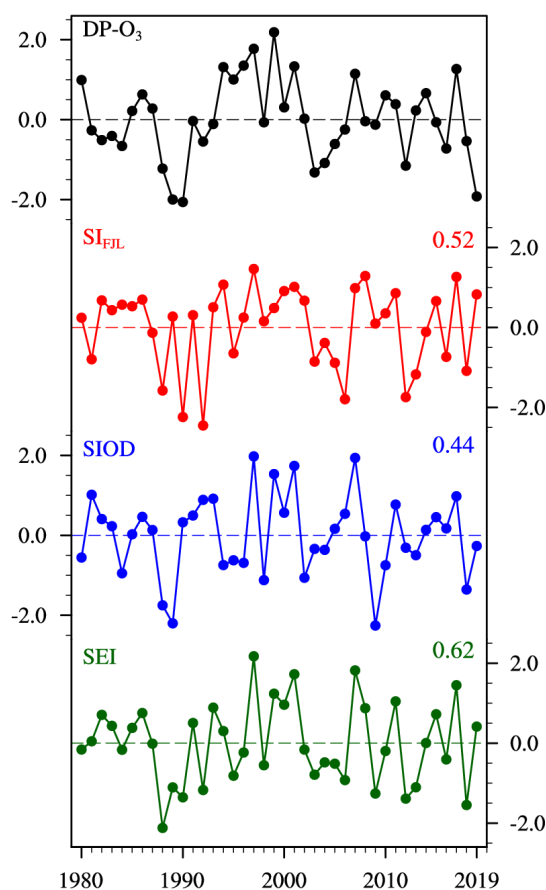
147 As aforementioned, the GEOS-Chem model has a good performance in simulating O<sub>3</sub> concentration.  
148 Therefore, the EOF approach was applied to the GEOS-Chem simulation for the period 1980–2019 to explore the  
149 dominant patterns of summer mean O<sub>3</sub> pollution in the east of China. Percentage contributions to the total variance  
150 by the first and second EOF modes were 39% and 17.5%, respectively. The significance test of the EOF  
151 eigenvalues confirmed that the first and second patterns were distinctly separated (passing the North test, North  
152 et al, 1982). The first EOF pattern displayed a monopole pattern (Figure S2). The second EOF pattern presented  
153 a north-south dipole pattern of O<sub>3</sub> (DP-O<sub>3</sub>) distribution in the east of China with the two centers located in NC  
154 and the Pearl River Delta (PRD, Figure 1b), respectively. Observations have shown that high O<sub>3</sub> concentration  
155 frequently occurs in NC, and O<sub>3</sub> pollution in the PRD has become increasingly serious in recent years (Liu et al.  
156 2020). Furthermore, about 80% of the MDA8 O<sub>3</sub> anomalies in NC were in opposite sign to those in PRD during  
157 2015–2019 (Figure S1a, b). Therefore, despite the fact that it was only the second leading EOF mode, we still  
158 focused on the investigation of DP-O<sub>3</sub> in the present study, since it was more similar to the actual pollution  
159 situation. Impacts of climate variability are also analyzed.

160 The MDA8 O<sub>3</sub> anomalies were divided into positive (P) and negative phases (N) of DP-O<sub>3</sub> (Figure S3). For  
161 convenience, DP-O<sub>3</sub>P and DP-O<sub>3</sub>N were defined by the EOF time series of DP-O<sub>3</sub> greater than 1 standard  
162 deviation and less than  $-1 \times$  standard deviation, respectively. The DP-O<sub>3</sub>P corresponded to positive anomalies of  
163 MDA8 O<sub>3</sub> in the north and negative anomalies in the PRD (Figure S3a). In contrast, high concentration of O<sub>3</sub>  
164 occurred in the PRD and low concentration center appeared in NC under the DP-O<sub>3</sub>N condition (Figure S3b). The  
165 correlation coefficient between time series of DP-O<sub>3</sub> and MDA8 O<sub>3</sub> difference between NC and the PRD was 0.91,  
166 indicating that DP-O<sub>3</sub> reflected the opposite changes of O<sub>3</sub> concentration in NC and the PRD.

167 With fixed emissions, the changes in O<sub>3</sub> concentrations from 1980 to 2019 were solely caused by  
168 meteorological conditions. The EOF time series of DP-O<sub>3</sub> showed a strong interannual variation (Figure 2).  
169 Composite differences in large-scale atmospheric circulation and meteorological condition related to DP-O<sub>3</sub>  
170 between the positive and negative phases (DP-O<sub>3</sub>P minus DP-O<sub>3</sub>N) were analyzed to explore the impacts of  
171 atmospheric circulation on photochemical reactions and accumulations of various pollutants in the above two  
172 areas. During the positive phase of DP-O<sub>3</sub>, cyclonic and anticyclonic anomalies in the middle troposphere were

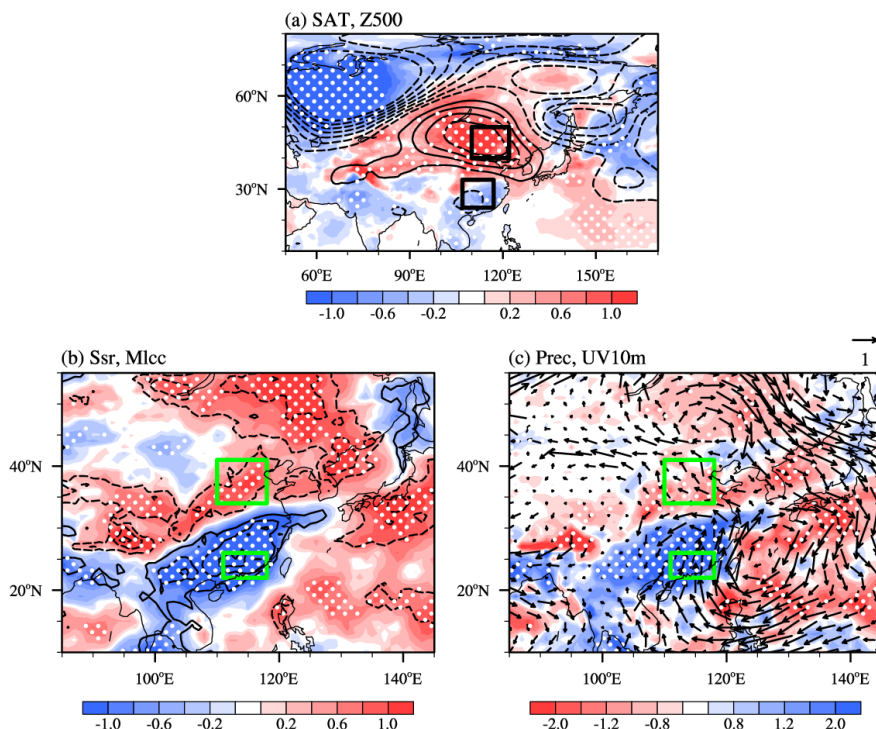


173 found over the PRD and NC ( $C_{PRD}$  and  $AC_{NC}$ ) (Figure 3a), respectively. The  $C_{PRD}$  and accompanied southerly  
174 winds in the PRD efficiently transported clean and moist air from the sea to the PRD (Figure 3c). Furthermore,  
175 low and medium cloud covers were significantly increased, which led to weak solar radiation and reduced  
176 photochemical reactions (Figure 3b). A moist, cool environment and weak solar radiation were conducive to low  
177  $O_3$  concentration in the PRD. On the other hand, the positive anomalies of geopotential height in NC increased  
178 surface air temperature (Figure 3a), resulting in a dry environment with decreased cloud covers and sunny weather  
179 (Figure 3b, c). Such kind of meteorological conditions was favorable for the generation of surface  $O_3$ , which  
180 explained why high MDA8  $O_3$  was occurred in NC. The above analysis revealed that large-scale atmospheric  
181 anomalies result in different meteorological conditions between NC and the PRD, and thus played an important  
182 role in the formation of the DP- $O_3$  pattern.



183

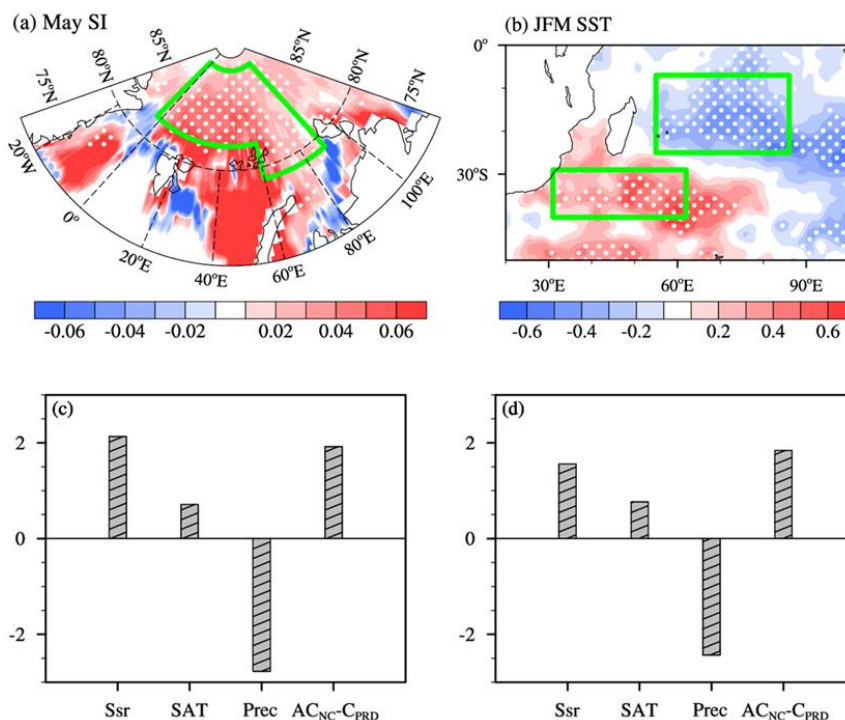
184 **Figure 2.** Variations in standardized DP- $O_3$  time series (black),  $S_{IFL}$  (red),  $S_{IOD}$  (blue), and SEI (green) from 1980 to 2019.  
185 The correlation coefficients of the DP- $O_3$  with  $S_{IFL}$  (red),  $S_{IOD}$  (blue), and SEI (green) were shown in the figure.



186

187 **Figure 3.** Composite summer atmospheric circulations associated with the DP-O<sub>3</sub> (DP-O<sub>3</sub>P minus DP-O<sub>3</sub>N) for the period  
188 1980 to 2019, including (a) SAT (unit: K, shadings) and geopotential height at 500 hPa (unit: gpm, contours), (b) Ssr (unit: 10<sup>6</sup>  
189 J m<sup>-2</sup>, shadings) and Mlcc (unit: 1, contours), and (c) Prec (unit: mm, shadings) and surface wind (unit: m s<sup>-1</sup>, arrows). The  
190 white dots indicate that the composites with shading were above the 90% confidence level. The black boxes in (a) indicate the  
191 centers of the AC<sub>NC</sub> and C<sub>PRD</sub>, respectively. The green boxes in (b) and (c) represent the areas of NC and the PRD.

192 Arctic SI in May was closely related to summer O<sub>3</sub> pollution in NC (Yin et al. 2019), but its effect on the  
193 north-south dipole distribution of O<sub>3</sub> had not been studied. The meridional O<sub>3</sub> dipole pattern in the east of China  
194 was positively correlated with SI anomalies near the Franz Josef Land (SI<sub>FJL</sub>). Note that the correlation between  
195 them remains unchanged after the signal of El Niño-Southern Oscillation (ENSO) was removed. The area-  
196 averaged (82–88°N, 3°W–60°E; 79–88°N, 60–90°E; denoted by the green boxes in Figure 4a) SI in May was  
197 calculated and defined as the SI<sub>FJL</sub> index, whose linear correlation coefficient with the time series of DP-O<sub>3</sub> was  
198 0.52 (exceeding the 99% confidence level). When the SI<sub>FJL</sub> anomalies were significant (i.e., |anomalies| > its one  
199 standard deviation), the occurrence probability of the DP-O<sub>3</sub> in the same phase was 83% (Figure 2). Furthermore,  
200 the active centers of the anomalous atmospheric circulations and meteorological conditions associated with SI<sub>FJL</sub>  
201 in the east of China were similar to that of the DP-O<sub>3</sub> (i.e., NC and PRD). That is, positive SI<sub>FJL</sub> anomalies were  
202 conducive to less (more) precipitation, less (more) cloud cover, and strong (weak) solar radiation in NC (PRD),  
203 and *vice versa* (Figure 4c, Figure S4).



204

205 **Figure 4.** Composites of (a) May SI concentration and (b) JFM SST associated with the DP-O<sub>3</sub> (DP-O<sub>3</sub>P minus DP-O<sub>3</sub>N) from  
 206 1980 to 2019. The green boxes in (a) and (b) indicate where the SI<sub>FJL</sub> and SIOD indices are calculated, respectively. The white  
 207 dots indicate that the composites were above the 90% confidence level. Composite summer meteorological conditions and  
 208 circulations associated with (c) SI<sub>FJL</sub> (positive SI<sub>FJL</sub> years minus negative SI<sub>FJL</sub> years) and (d) SIOD (positive SIOD years  
 209 minus negative SIOD years) from 1980 to 2019, including the differences in Ssr (unit:  $10^6 \text{ J m}^{-2}$ ), SAT (unit: K), and Prec (unit:  
 210 mm) between NC and the PRD (NC minus PRD), and the differences between AC<sub>NC</sub> and C<sub>PRD</sub>. The black slashes indicate that  
 211 the composites were above the 90% confidence level.

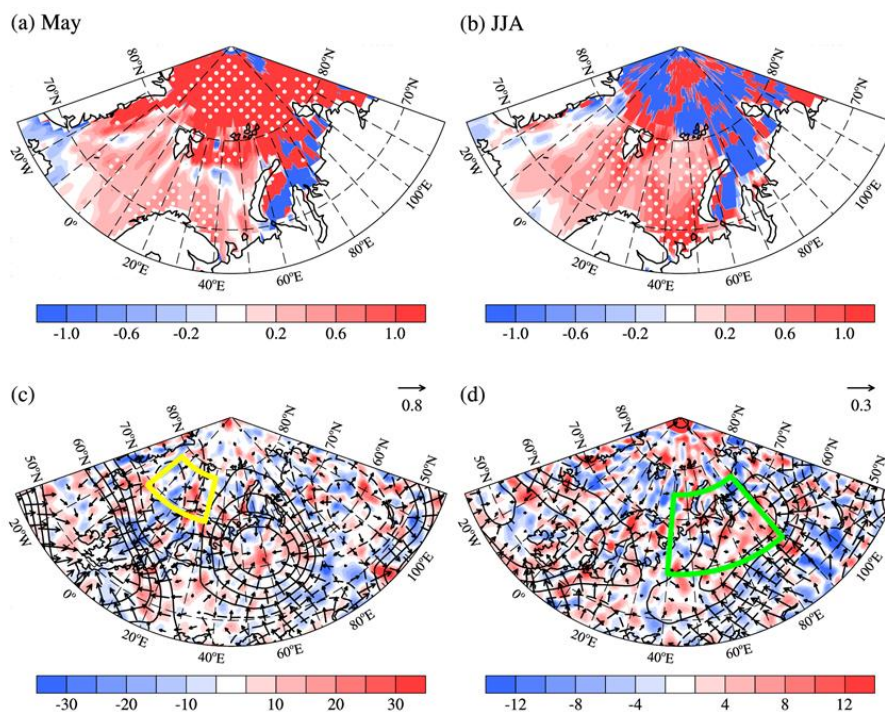
212 In addition to the signal from the Arctic, SST as an effective external forcing also has significant influences  
 213 on summer climate in the east of China (Li et al. 2018). Therefore, it was important to answer the question whether  
 214 SST could affect the DP-O<sub>3</sub> in the east of China in summer. Large anomalies of preceding January–February–  
 215 March (JFM) SST over the southern Indian Ocean was obvious when we evaluated the relationship between the  
 216 DP-O<sub>3</sub> and previous SST. After removing the influence of ENSO, the SST signal in the southern Indian Ocean  
 217 still maintains (Figure 4b). The two regions with significant anomalies were similar to the Subtropical Indian  
 218 Ocean Dipole (SIOD) regions found by Behera and Yamagata (2001). Variance analysis and correlation analysis  
 219 of SST in the Indian Ocean also indicated that a SST dipole type oscillation occurred in the southern Indian Ocean,  
 220 which usually developed in the preceding winter and reaches its strongest in the subsequent January to March (Jia  
 221 and Li 2013). The difference between the mean SST of the two regions (29–40°S, 31–62°E and 7–25°S, 55–86°E;  
 222 green box in Figure 4b; the southwest positive pole minus the northeast negative pole) was defined as the SIOD



223 index and calculated (Figure 2). The linear correlation coefficient between the SIOD index and the time series of  
224 DP-O<sub>3</sub> from 1980 to 2019 was 0.44 (significant at the 99% confidence level). When the SIOD anomalies were  
225 significant (i.e., |anomalies| > its one standard deviation), the occurrence probability of DP-O<sub>3</sub> in the same phase  
226 is 82% (Figure 2). Furthermore, the composite meteorological conditions in the positive and negative phases of  
227 SIOD had similar active centers to that of DP-O<sub>3</sub>. That is, the anticyclone over NC was always accompanied by  
228 hot-dry meteorological condition, while the cyclone over PRD was always accompanied by cool-moist  
229 environment (Figure 4d; Figure S5).

#### 230 **4. Associated physical mechanisms**

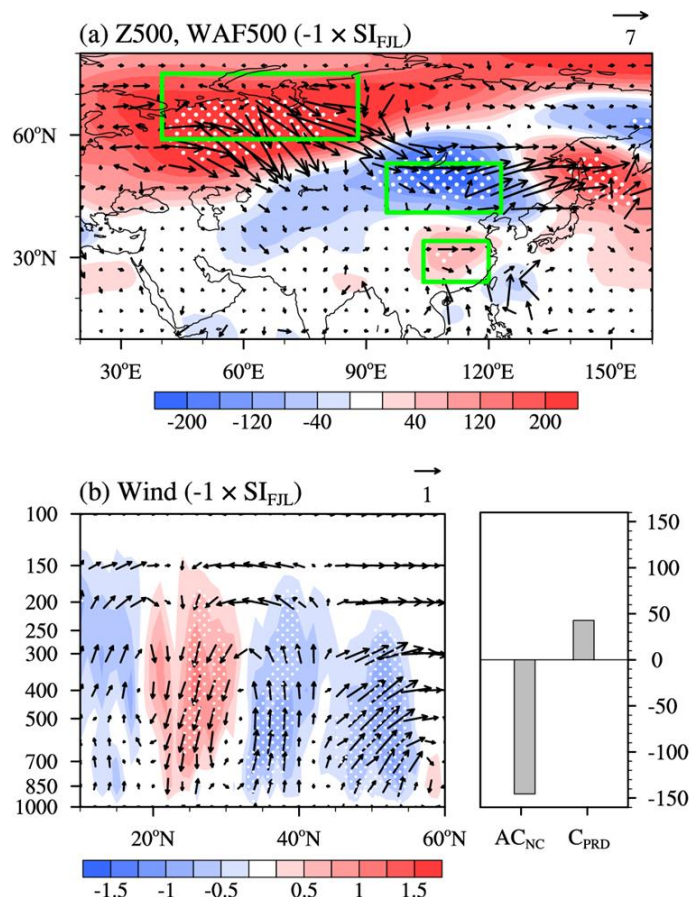
231 Changes in SI<sub>FJL</sub> and SIOD both could possibly contribute to the formation of DP-O<sub>3</sub>. Note that the  
232 correlation coefficient between them was only 0.21 and was not significant, indicating that SI<sub>FJL</sub> and SIOD were  
233 independent of each other. Several previous studies have documented that the preceding Arctic SI anomalies could  
234 trigger EU-like atmospheric responses in the subsequent summer, and thus influenced the climate in the east of  
235 China (Wang and He 2015). Corresponding to reduced SI<sub>FJL</sub>, SST anomalies in the Barents and Kara Sea were  
236 significantly positive and gradually increase from May to summer months (Figure 5a, b). The warm SST  
237 anomalies influenced local heat anomalies and caused anomalous atmospheric circulations. Following the  
238 decrease in SI<sub>FJL</sub>, anomalous divergent winds appeared in the mid-troposphere, which were accompanied by warm  
239 SST anomalies and negative velocity potential anomalies (yellow box in Figure 5c). As proposed by Xu et al.,  
240 (2021), the rotational component of the anomalous divergent winds could spread to the south and force the  
241 vorticity generation over Eurasia. Thus, during the subsequent summer, significant convergence and positive  
242 velocity potential with a positive Rossby wave source anomaly occurred over northern Europe and West Siberia  
243 (green box in Figure 5d). We also used the SST anomalies associated with SI<sub>FJL</sub> (in Barents and Kara Sea in JJA)  
244 to composite relevant variables. Significant convergence, positive velocity potential, and positive Rossby source  
245 anomaly all appeared over Europe and West Siberia in JJA (Figure S6). This indicated that positive anomalies of  
246 Rossby-wave source over Europe and West Siberia could be generated by local heat anomalies associated with  
247 decreased SI<sub>FJL</sub> in the Barents and Kara Sea.



248

249 **Figure 5.** Composites of (a) May Arctic SST (unit: K) and (c) Rossby wave source anomalies at 500 hPa (unit:  $10^{-11} \text{ s}^{-2}$ )  
250 associated with  $SI_{FJL}$  index (negative  $SI_{FJL}$  years minus positive  $SI_{FJL}$  years) from 1980 to 2019. (b, d) same as (a, c) but for  
251 JJA. The shadings, contours and vectors in (c, d) represent Rossby wave source, velocity potential (unit:  $10^5 \text{ m}^2 \text{ s}^{-1}$ ) and  
252 divergent wind (unit:  $\text{m s}^{-1}$ ), respectively. The yellow box in (c) and green box in (d) represents the center of the velocity  
253 potential and Rossby wave source anomaly associated with  $SI_{FJL}$ , respectively. The white dots indicate that the composites  
254 with shading were above the 90% confidence level.

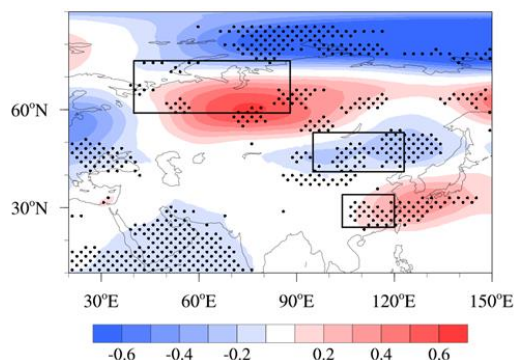
255 Moreover, corresponding to the decreased  $SI_{FJL}$ , the anomalous Rossby WAF propagated from Europe and  
256 West Siberia (consistent with the aforementioned Rossby wave source) to Northeast China and enhanced the  
257 cyclonic anomaly nearby (Figure 6a). The anomalous cyclonic circulation caused ascending motion from the  
258 surface up to 300 hPa over NC, and further induced a meridional circulation with an anomalous descending branch  
259 near  $20^\circ\text{N}$  (Figure 6b). Likewise, an anomalous anticyclone occurred in the middle troposphere above the PRD  
260 (Figure 6b). In other words, an EU-like Rossby wave train was induced in the mid-troposphere (Figure 6a), which  
261 propagated from northern Europe and West Siberian Plain (+), reaching the broad area from northeastern China  
262 (-) to the south of China (+). Thus, the reduction in SI near the Franz Josef Land in the May modulated the EU-  
263 like pattern in the subsequent summer and strengthened the anomalous cyclonic and anticyclonic circulations over  
264 NC and the PRD (Figure 6b), respectively. The differences in anomalous atmospheric circulations and associated  
265 meteorological conditions between NC and the PRD make great contributions to the occurrence of DP- $\text{O}_3$ .



266

267 **Figure 6.** Composites of (a) wave activity flux anomalies (unit:  $\text{m}^2 \text{s}^{-2}$ , arrows), geopotential height (unit: gpm, shading) at  
268 500 hPa and (b) mean wind (unit:  $\text{m s}^{-1}$ , arrows), omega (unit:  $10^{-2} \text{ Pa s}^{-1}$ , shading) over 100–130° E, and the anomalies of  
269 AC<sub>NC</sub> and C<sub>PRD</sub> (unit: gpm, bar) in summer associated with SI<sub>FJL</sub> index (negative SI<sub>FJL</sub> years minus positive SI<sub>FJL</sub> years) from  
270 1980 to 2019. The green boxes in (a) represent the centers of the EU-like pattern. The white dots indicate that the composites  
271 with shading were above the 90% confidence level.

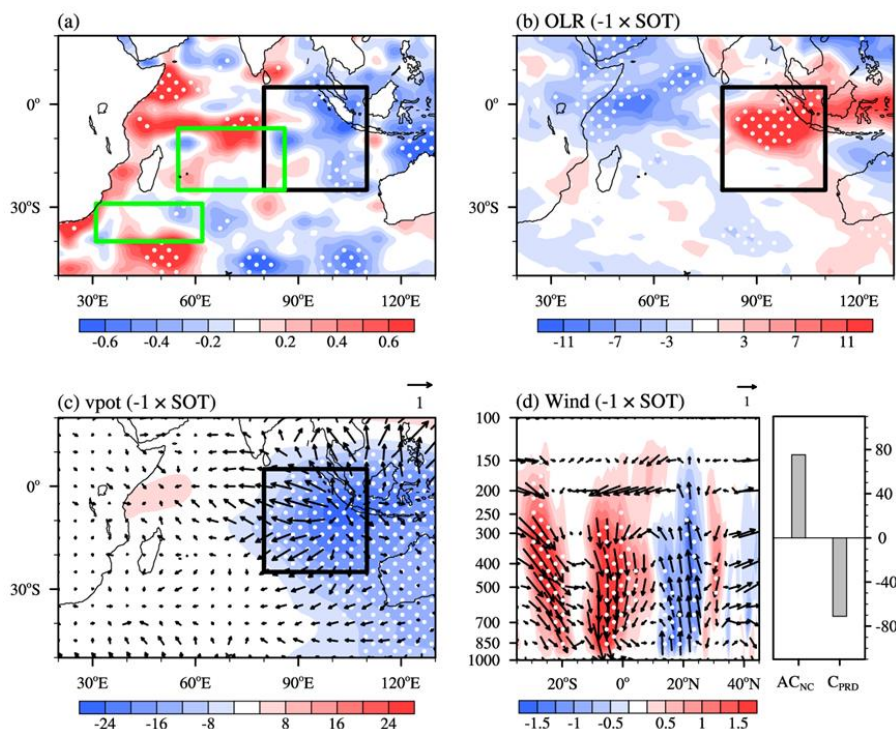
272 The relationship between the preceding May SI anomalies and the JJA EU-like pattern was also confirmed  
273 by large ensemble simulations of CESM. According to the simulated sea ice fraction near the Franz Josef Land,  
274 the three years with the lowest and highest SI in each member were selected to construct the composite maps  
275 based on all the 40 available members. The difference in JJA geopotential height at 500 hPa represented the  
276 atmospheric response to declining May SI<sub>FJL</sub>. As shown in Figure 7, the decline of SI<sub>FJL</sub> in May led to an EU-like  
277 pattern in the subsequent summer over Eurasia, which was in good accordance with the observed result (Figure  
278 6a). The anticyclonic and cyclonic anomalies shown in the geopotential height at 500 hPa (i.e., AC<sub>NC</sub> and C<sub>PRD</sub>)  
279 in summer were also well reproduced by over 60% of the members. The above results confirmed the robustness  
280 of the physical mechanisms proposed in the present study.



281

282 **Figure 7.** Composite differences of geopotential height at 500 hPa in JJA between three low and high SIFIL years based on the  
283 ensemble of 40 CESM-LE simulations during 1980–2019. The black dots indicate that the mathematical sign of the composite  
284 results of more than 60 % of the members is consistent with the ensemble mean. The black boxes represent the centers of the  
285 EU-like pattern.

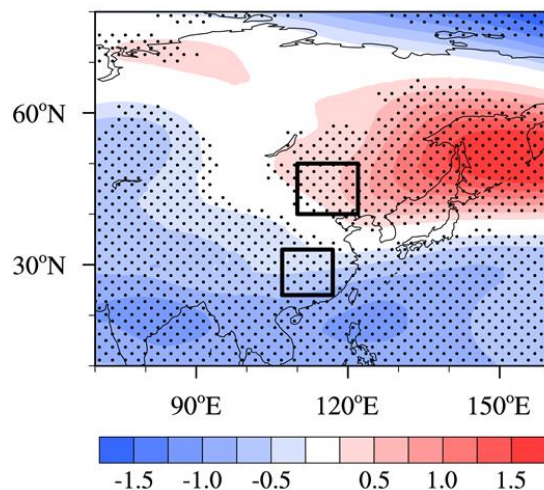
286 SIOD could influence atmospheric anomalies and distribution of summer precipitation in China mainly  
287 through Hadley circulation (Liu et al. 2019). Can SIOD anomalies also influenced the DP-O<sub>3</sub> via meridional  
288 atmospheric forcing? Despite the significant correlation between SIOD anomalies (defined by SST) and the DP-  
289 O<sub>3</sub> in the east of China (Figure 4b), it should be noted that the thermodynamic signals in the southern Indian Ocean  
290 not only existed on the sea surface but also extended to the subsurface (Figure S7). As time goes by, the center of  
291 negative SST anomalies moved to the northeast possibly due to the eastward movement of atmospheric forcing  
292 caused by the mean westerly flow (Behera and Yamagata 2001). When it moved to the vicinity of Sumatra Island  
293 in JJA, the abnormally cold signals of SST could extend downward from the surface to 60m (black box in Figure  
294 8a). The area-averaged (black box in Figure 8a) summer-mean subsurface ocean temperature of 0–60m was  
295 defined as the SOT index and calculated. Affected by negative SOT anomalies near Sumatra Island, the equatorial  
296 eastern Indian Ocean convection was suppressed (indicated by positive anomalies of OLR in Figure 8b) and  
297 significant divergence prevailed in the lower troposphere (Figure 8c). As a result, anomalous downward air flow  
298 developed near Sumatra Island from 300 hPa to the surface (about 20–5°S in Figure 8d). This anomalous  
299 downward air flow modulated the meridional circulation over 90–120 °E by strengthening the abnormal upward  
300 airflow at 20°N and downward airflow at 30°N. Thus, the AC<sub>NC</sub> and C<sub>PRD</sub> were enhanced simultaneously (Figure  
301 8d). Overall, following the positive phase of SIOD, the cold signal of SOT anomalies changed the meridional  
302 circulation in the subsequent JJA and strengthened the C<sub>PRD</sub> and AC<sub>NC</sub> in the troposphere above the east of China.  
303 Under these large-scale atmospheric anomalies, O<sub>3</sub> concentrations became higher in NC, whereas the generation  
304 of surface O<sub>3</sub> were weakened in the PRD.



305

306 **Figure 8.** (a) Composites of mean 0–60m subsurface ocean temperature (unit: K) in summer associated with the SIOD  
307 (positive SIOD years minus negative SIOD years) from 1980 to 2019. The green boxes represent the centers of the SIOD, and  
308 the black box indicates where the SOT index is calculated. Composites of (b) OLR (unit:  $\text{W m}^{-2}$ ) and (c) velocity potential  
309 (unit:  $10^5 \text{ m}^2 \text{ s}^{-1}$ , shadings) and divergent winds (unit:  $\text{m s}^{-1}$ , vectors) at 1000 hPa in summer associated with SOT indexes of  
310 opposite sign (negative SOT years minus positive SOT years). The black box represents the center of the SOT. (d) Composites  
311 of summer mean winds (unit:  $\text{m s}^{-1}$ , arrows) and omega (unit:  $10^{-2} \text{ Pa s}^{-1}$ , shadings) over 90–120°E, and the anomalies of  $AC_{NC}$   
312 and  $C_{PRD}$  (unit: gpm, bars) associated with SOT indexes of opposite sign. The white dots indicate that the composites with  
313 shading were above the 90% confidence level.

314 The CESM-LE datasets were also used to verify the statistical correlation between the preceding SIOD and  
315 large-scale atmospheric circulations in JJA. The composite differences of SIOD in JFM between the three high  
316 years and three low years of SI simulated by each ensemble member during 1980–2019 were investigated based  
317 on the ensemble of 40 CESM-LE simulations. The composite results (positive SIOD years minus negative SIOD  
318 years) of atmospheric circulations could be considered as the relevant atmospheric circulation responses  
319 associated with differences in SIOD. More than 60% of the CESM ensemble members could well reproduce the  
320 anticyclonic circulation over NC and the cyclonic circulation over the PRD in summer at 500hPa (Figure 9). That  
321 is, the CESM-LE also confirmed the relationship between the previous JFM SIOD anomaly and the DP- $\text{O}_3$ -related  
322 atmospheric circulations (i.e.,  $AC_{NC}$  and  $C_{PRD}$ ) in subsequent JJA.



323

324 **Figure 9.** Composite differences of geopotential height at 500 hPa in JJA between three high and low SIOD years based on  
325 the ensemble of 40 CESM-LE simulations during 1980–2019. The black dots indicate that the mathematical sign of the  
326 composite results of more than 60 % of the members is consistent with the ensemble mean. The black boxes represent the  
327 centers of  $AC_{NC}$  and  $C_{PRD}$ , respectively.

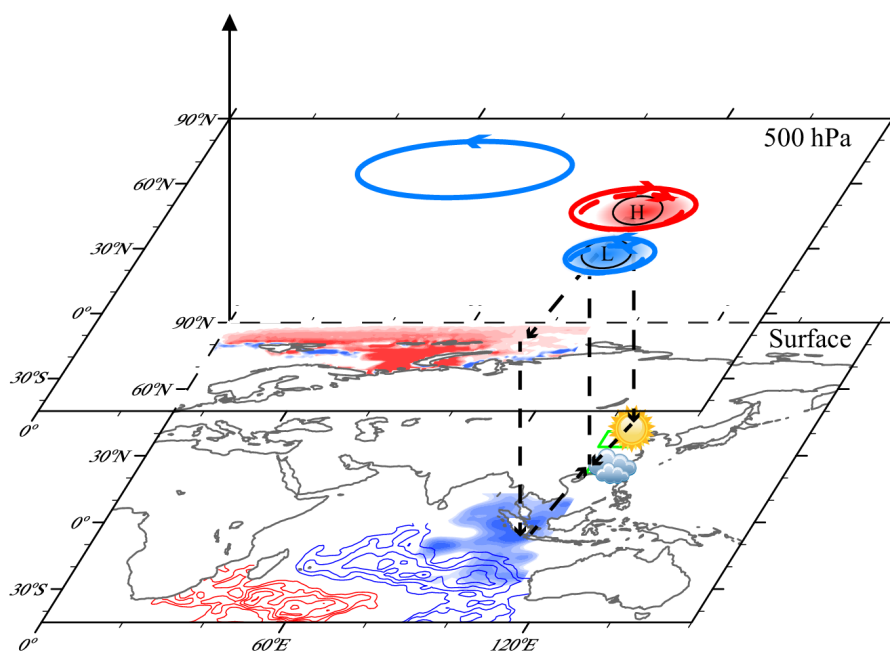
## 328 5. Conclusions and discussions

329 In general, the  $O_3$  concentrations in NC were substantially high and the problem of  $O_3$  pollution in the PRD  
330 has become increasingly prominent in recent years. A south-north dipole pattern of  $O_3$  concentration in the east of  
331 China was identified based on GEOS-Chem simulations with fixed emissions and changing meteorological  
332 condition from 1980 to 2019. The DP- $O_3$  pattern presented opposite centers in NC and PRD. Corresponding to  
333 the positive phase of DP- $O_3$ , cyclonic and anticyclonic anomalies were located over the PRD and NC respectively,  
334 which resulted in dry and hot climate in NC, while the environment in the PRD region was cool and moist. The  
335 opposite was true in the negative phase of DP- $O_3$ . During positive phases, the meteorological condition mentioned  
336 above significantly enhanced natural emissions of  $O_3$  precursors and photochemical reactions in NC but  
337 suppressed  $O_3$  production in the PRD, and thus make great contributions to the south-north dipole pattern of  $O_3$   
338 in the east of China.

339 Arctic SI near the Franz Josef Land in May played an important role in the occurrence of DP- $O_3$ . The warm  
340 SST anomalies associated with less  $SI_{FJL}$  could induce divergent wind field and vorticity advection in the upper  
341 layer, and enhanced positive Rossby wave source over northern Europe and West Siberia in summer. An EU-like  
342 pattern was triggered in Eurasia (solid lines in Figure 10), which could enhance the DP- $O_3$ -related atmospheric  
343 circulation (i.e.,  $AC_{NC}$  and  $C_{PRD}$ ) in JJA. As a result, meteorological conditions for  $O_3$  concentration were  
344 completely different between NC and PRD, which eventually contributed the formation of DP- $O_3$ . In addition, the



345 precursory climatic driving signal of SIOD anomalies in the low latitudes in JFM was also closely linked to DP-  
346 O<sub>3</sub>. The thermodynamic signal of SIOD could be stored in the subsurface, and the center of negative SST  
347 anomalies moved to the vicinity of Sumatra Island in summer. The meridional circulation intensified in summer  
348 (dashed lines in Figure 10), which, along with the enhancement of the AC<sub>NC</sub> and C<sub>PRD</sub> over the east of China,  
349 effectively increased O<sub>3</sub> concentration in NC but suppressed the generation of surface O<sub>3</sub> in the PRD. The linkages  
350 and corresponding physical mechanisms were well reproduced by the large CESM-LE ensemble simulation.



351

352 **Figure 10.** Schematic diagrams of the associated physical mechanisms. The May SI anomalies near the Franz Josef Land (red  
353 shadings) could trigger an EU-like pattern in the atmosphere in summer, which enhances the anticyclonic anomaly over NC  
354 and the cyclonic anomaly over the PRD. The thermodynamic signal of the preceding SIOD (contours) could be stored in the  
355 subsurface and the center of negative SST anomalies moves to the vicinity of Sumatra Island in summer (blue shading). The  
356 meridional circulation was enhanced in summer (dashed lines), along with the enhancement of AC<sub>NC</sub> and C<sub>PRD</sub> over eastern  
357 China. The solid lines indicate the anomalous atmospheric circulations affected by SI<sub>FJL</sub>, while the dashed lines indicate the  
358 anomalous atmospheric circulations affected by SIOD.

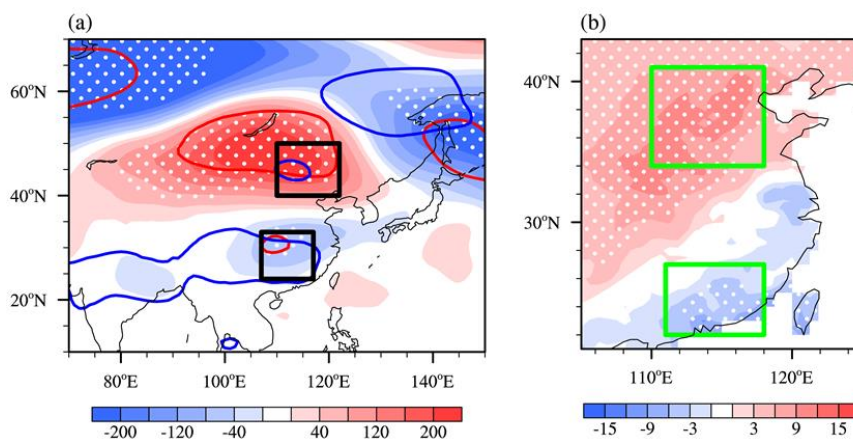
359 The above analysis has revealed that the DP-O<sub>3</sub> is independently affected by SIOD and SI<sub>FJL</sub> from 1980 to  
360 2019. We attempted to discuss the combined impacts of the two precursory climatic drivers in the present  
361 study. For this purpose, a synthetic climate variability index SEI, defined as the weighted average of SI<sub>FJL</sub> and  
362 SIOD, is calculated by

363

$$SEI = \frac{r_1 \times SI_{FJL} + r_2 \times SIOD}{|r_1| + |r_2|}$$



364 where  $r_1$  and  $r_2$  were the correlation coefficients of  $SI_{FJL}$  ( $r_1 = 0.52$ ) and SIOD ( $r_2 = 0.44$ ) with the DP- $O_3$   
365 time series, respectively. The correlation coefficient between SEI and DP- $O_3$  was 0.62 (Figure 2, exceeding the  
366 99% confidence level). When the SEI anomalies were significant, the occurrence probability of the DP- $O_3$  in the  
367 same phase was 93% (Figure 2), which is higher than that based on individual influences of the two factors.  
368 Composite atmospheric circulation analysis has been carried out based on years of positive and negative SEI  
369 anomalies, and the results are shown in Figure 11a. The composite atmospheric circulation based on the SEI index  
370 was stronger, resulting in the concentrations of MDA8  $O_3$  in NC was  $11.74 \mu\text{g m}^{-3}$  higher than that in PRD (Figure  
371 11b). The main areas influenced by SI and SST were slightly different. Although the two precursory climatic  
372 drivers both could affect the atmospheric circulations over NC and the PRD,  $SI_{FJL}$  mainly affected atmospheric  
373 circulation anomaly over NC, while SIOD played a major role in the PRD. However, climate variabilities at  
374 different latitudes jointly facilitated the dipole pattern of  $O_3$  in the east of China from 1980 to 2019.



375

376 **Figure 11.** (a) Composites of geopotential height at 500 hPa (unit: gpm, shadings) in summer associated with the SEI (positive  
377 SEI years minus negative SEI years) from 1980 to 2019. The red and blue lines indicate areas where the composite  
378 geopotential height anomalies associated with  $SI_{FJL}$  and SIOD exceed the 90% confidence level, respectively. The black boxes  
379 represent the centers of  $AC_{NC}$  and  $C_{PRD}$ , respectively. (b) Composite differences of the detrended summer-mean MDA8  $O_3$   
380 (unit:  $\mu\text{g m}^{-3}$ ) simulated by GEOS-Chem model between high and low SEI years during 1980–2019. The white dots indicate  
381 that the composite differences are above the 90% confidence level. The green boxes represent the areas of NC and the PRD.

382 The north-south dipole pattern of  $O_3$  in the east of China in summer and its relationship with climate factors were  
383 clearly revealed in this study, yet some questions still remain unanswered and should be investigated in the future.  
384 The GEOS-Chem model simulations were used to explore the dominant pattern of  $O_3$  in the east of China in  
385 summer due to the short sequence of  $O_3$  observations. Although the GEOS-Chem demonstrated a good  
386 performance based on evaluation, there still exist some differences between the simulations and observations. In  
387 addition, statistical and numerical methods were used to reveal and verify the physical mechanisms behind the



388 dipole pattern of O<sub>3</sub> in the east of China and its relation with climate variability. However, further numerical  
389 experiments should be carried out in the future. For example, coupled climate-chemistry models should be used  
390 to not only simulated the influence of climate driving factors on O<sub>3</sub> pattern, but also revealed the effect of  
391 individual climate factors as well as their comprehensive effects.

392

393

394 **Data Availability.** Hourly O<sub>3</sub> concentration data could be downloaded from <https://quotsoft.net/air/> (Ministry of  
395 Environmental Protection of China, the last accessible data are for 23 September 2020). Sea ice concentration,  
396 sea surface temperature, and subsurface ocean temperature data were from <https://www.metoffice.gov.uk/hadobs/>  
397 (Met Office Hadley Centre, 2020). Monthly ERA5 reanalysis dataset was available at  
398 <https://cds.climate.copernicus.eu/cdsapp#!/home> (Copernicus Climate Change Service. The last accessible data  
399 were for 4 March 2021). The monthly OLR data could be acquired from <http://olr.umd.edu/> (University of  
400 Maryland OLR Climate Data Record portal).

401

#### 402 **Acknowledgements**

403 This work was supported by National Natural Science Foundation of China (42088101, 41991280, 42025502 and  
404 91744311).

405

#### 406 **Authors' contribution**

407 Yin Z. C. designed the research. Ma X. Q. performed the research and analyzed the data. Yin Z. C. and Ma X. Q.  
408 prepared the manuscript.

409

#### 410 **Competing interests**

411 The authors declare no conflict of interest.



412 **References**

- 413 Behera, S. K., and Yamagata, T.: Subtropical SST dipole events in the southern Indian Ocean, *Geophys. Res. Lett.*,  
414 28, 327–330, <https://doi.org/10.1029/2000GL011451>, 2001.
- 415 Bey, I., Jacob, D. J., Yantosca, R. M., Logan, J. A., Field, B., Fiore, A. M., Li, Q., Liu, H., Mickley, L. J., and  
416 Schultz, M.: Global modeling of tropospheric chemistry with assimilated meteorology: Model description and  
417 evaluation, *J. Geophys. Res.*, 106, 23073–23095, <https://doi.org/10.1029/2001JD000807>, 2001.
- 418 Chen, Z. Y., Zhuang, Y., Xie, X. M., Chen, D. L., Cheng, N. L., Yang, L., and Lia, R. Y.: Understanding long-  
419 term variations of meteorological influences on ground ozone concentrations in Beijing During 2006–2016,  
420 *Environ. Pollut.*, 245, 29–37, <https://doi.org/10.1016/j.envpol.2018.10.117>, 2019.
- 421 Gelaro, R., McCarty, W., Suarez, M. J., Todling, R., Molod, A., Takacs, L., Randles, C. A., Darmenov, A.,  
422 Bosilovich, M. G., Reichle, R., Wargan, K., Coy, L., Cullather, R., Draper, C., Akella, S., Buchard, V., Conaty, A.,  
423 da Silva, A. M., Gu, W., Kim, G. K., Koster, R., Lucchesi, R., Merkova, D., Nielsen, J. E., Partyka, G., Pawson, S.,  
424 Putman, W., Rienecker, M., Schubert, S. D., Sienkiewicz, M., and Zhao, B.: The Modern-Era Retrospective Analysis  
425 for Research and Applications, Version 2 (MERRA2), *J. Climate*, 30, 5419–5454, [https://doi.org/10.1175/jcli-d-](https://doi.org/10.1175/jcli-d-160758.1)  
426 160758.1, 2017.
- 427 Good, S. A., Martin, M. J., and Rayner, N. A.: EN4: quality controlled ocean temperature and salinity profiles and  
428 monthly objective analyses with uncertainty estimates, *J. Geophys. Res. Oceans*, 118, 6704–  
429 6716, <https://doi.org/10.1002/2013JC009067>, 2013.
- 430 Han, H., Liu, J., Shu, L., Wang, T. J., and Yuan, H. L.: Local and synoptic meteorological influences on daily  
431 variability in summertime surface ozone in eastern China, *Atmos. Chem. Phys.* 20, 203–222,  
432 <https://doi.org/10.5194/acp-20-203-2020>, 2020.
- 433 Han, J. P., and Zhang, R. H.: The Dipole Mode of the Summer Rainfall over East China during 1958–2001, *Adv.*  
434 *Atmos. Sci.*, 26, 727–735, <https://doi.org/10.1007/s00376-009-9014-6>, 2009.
- 435 Hersbach, H., Bell, B., Berrisford, P., Hirahara, S., Horányi, A., Muñoz-Sabater, J., Nicolas, J., Peubey, C., Radu,  
436 R., Schepers, D., Simmons, A., Soci, C., Abdalla, S., Abellan, X., Balsamo, G., Bechtold, P., Biavati, G., Bidlot,  
437 J., Bonavita, M., De Chiara, G., Dahlgren, P., Dee, D., Diamantakis, M., Dragani, R., Flemming, J., Forbes, R.,  
438 Fuentes, M., Geer, A., Haimberger, L., Healy, S., Hogan, R. J., Hólm, E., Janisková, M., Keeley, S., Laloyaux, P.,  
439 Lopez, P., Lupu, C., Radnoti, G., de Rosnay, P., Rozum, I., Vamborg, F., Villaume, S., and Thépaut, J.-N.: The  
440 ERA5 global reanalysis, *Q. J. Roy. Meteor. Soc.*, 146, 1999–2049, <https://doi.org/10.1002/qj.3803>, 2020.
- 441 Jia, X. L., and Li, C. Y.: Dipole oscillation in the Southern Indian Ocean and its impacts on climate, *Chinese J.*  
442 *Geophys.*, 48, 1323–1335, <https://doi.org/10.1002/cjg2.780>, 2013.
- 443 Kay, J. E., Deser, C., Phillips, A., Mai, A., Hannay, C., Strand, G., Arblaster, J., Bates, S., Danabasoglu, G.,  
444 Edwards, J., Holland, M., Kushner, P., Lamarque, J.-F., Lawrence, D., Lindsay, K., Middleton, A., Muñoz, E.,  
445 Neale, R., Oleson, K., Polvani, L., and Vertenstein, M.: The Community Earth System Model (CESM) Large  
446 Ensemble Project: A community resource for studying climate change in the presence of internal climate  
447 variability, *B. Am. Meteorol. Soc.*, 96, 1333–1349, <https://doi.org/10.1175/BAMS-D-13-00255.1>, 2015.



- 448 Li, H. X., Sun, B., Zhou, B. T., Wang, S. Z., Zhu, B. Y., and Fan, Y.: Effect of the Barents Sea ice in March on the  
449 dipole pattern of air temperature in August in eastern China and the corresponding physical mechanisms, *Trans*  
450 *Atmos Sci*, 44, 89–103, <https://doi.org/10.13878/j.cnki.dgkxxb.20130427001>, 2021.
- 451 Li, K., Jacob, D.J., Liao, H., Zhu, J., Shah, V., Shen, L., Bates, K. H., Zhang, Q., and Zhai, S. X.: A two-pollutant  
452 strategy for improving ozone and particulate matter air quality in China, *Nat. Geosci.*, 12, 906–910,  
453 <https://doi.org/10.1038/s41561-019-0464-x>, 2019.
- 454 Li, S. P., Wei, H., and Feng, G. L.: Atmospheric Circulation Patterns over East Asia and Their Connection with  
455 Summer Precipitation and Surface Air Temperature in Eastern China during 1961–2013, *J Meteorol Res*, 32, 203–  
456 218, <https://doi.org/10.1007/s13351-018-7071-4>, 2018.
- 457 Li, Z. Q., and Xiao, Z. N.: Thermal contrast between the Tibetan Plateau and tropical Indian Ocean and its  
458 relationship to the South Asian summer monsoon, *Atmos Ocean Sci Lett*, 14, 100002,  
459 <https://doi.org/10.1016/j.aosl.2020.100002>, 2021.
- 460 Liu, H. L., Zhang, M. G., and Han, X.: A review of surface ozone source apportionment in China, *Atmos Ocean*  
461 *Sci Lett*, 13, 470–484, <https://doi.org/10.1080/16742834.2020.1768025>, 2020.
- 462 Liu, L., Guo, J. P., Chen, W., Wu, R. G., Wang, L., Gong, H. N., Liu, B., Chen, D. D., and Li, J.: Dominant  
463 Interannual Covariations of the East Asian-Australian Land Precipitation during Boreal Winter, *J. Climate*, 32,  
464 3279–3296, <https://doi.org/10.1175/JCLI-D-18-0477.1>, 2019.
- 465 Lin, Z. D., and Li, F.: Impact of interannual variations of spring sea ice in the Barents Sea on East Asian rainfall  
466 in June, *Atmos Ocean Sci Lett*, 11, 275–281, <https://doi.org/10.1080/16742834.2018.1454249>, 2018.
- 467 Lu, X., Zhang, L., Chen, Y., Zhou, M., Zheng, B., Li, K., Liu, Y., Lin, J., Fu, T.-M., and Zhang, Q.: Exploring  
468 2016–2017 surface ozone pollution over China: source contributions and meteorological influences, *Atmos. Chem.*  
469 *Phys.*, 19, 8339–8361, <https://doi.org/10.5194/acp-19-8339-2019>, 2019.
- 470 North, G. R., Bell, T. L., Cahalan, R. F., and Moeng, F. J.: Sampling errors in the estimation of empirical  
471 orthogonal functions *Mon. Weather Rev.*, 110, 699–706, [https://doi.org/10.1175/1520-0493\(1982\)110<0699:SEITEO>2.0.CO;2](https://doi.org/10.1175/1520-0493(1982)110<0699:SEITEO>2.0.CO;2), 1982.
- 473 Pu, X., Wang, T. J., Huang, X., Melas, D., Zanis, P., Papanastasiou, D. K., and Poupkou, A.: Enhanced surface  
474 ozone during the heat wave of 2013 in yangtze river delta region, china, *Sci. Total Environ.*, 603, 807–  
475 816, <https://doi.org/10.1016/j.scitotenv.2017.03.056>, 2017.
- 476 Rayner, N. A., Parker, D. E., Horton, E. B., Folland, C. K., Alexander, L. V., Rowell, D. P., Kent, E. C., and Kaplan,  
477 A.: Global analyses of sea surface temperature, sea ice, and night marine air temperature since the late nineteenth  
478 century, *J. Geophys. Res.*, 108, 4407, <https://doi.org/10.1029/2002JD002670>, 2003.
- 479 Rider, C. F., and Carlsten, C.: Air pollution and DNA methylation: effects of exposure in humans, *Clin Epigenetics*,  
480 11, 131, <https://doi.org/10.1186/s13148-019-0713-2>, 2019.
- 481 Sardeshmukh, P. D., and Hoskins, B. J.: The generation of global rotational flow by steady idealized tropical  
482 divergence, *J. Atmos. Sci.*, 45, 1228–1251, [https://doi.org/10.1175/1520-0469\(1988\)045<1228:TGOGRF>2.0.CO;2](https://doi.org/10.1175/1520-0469(1988)045<1228:TGOGRF>2.0.CO;2), 1988.



- 484 Takaya, K., and Nakamura, H.: A Formulation of a Phase-Independent Wave-Activity Flux for Stationary and  
485 Migratory Quasigeostrophic Eddies on a Zonally Varying Basic Flow, *J. Atmos. Sci.*, 58, 608-627,  
486 [https://doi.org/10.1175/1520-0469\(2001\)058<0608:AFOAPI>2.0.CO;2](https://doi.org/10.1175/1520-0469(2001)058<0608:AFOAPI>2.0.CO;2), 2001.
- 487 Tian, B., and Fan, K.: Climate prediction of summer extreme precipitation frequency in the Yangtze River valley  
488 based on sea surface temperature in the southern Indian Ocean and ice concentration in the Beaufort Sea, *Int. J.*  
489 *Climatol.*, 40, 4117–4130, <https://doi.org/10.1002/joc.6446>, 2019.
- 490 Wang, H., and He, S.: The North China/northeastern Asia severe summer drought in 2014, *J. Climate*, 28, 6667–  
491 6681, <https://doi.org/10.1175/JCLI-D-15-0202.1>, 2015.
- 492 Wang, J., and Guo, Y.: Possible impacts of Barents Sea ice on the Eurasian atmospheric circulation and the rainfall  
493 of East China in the beginning of summer, *Adv Atmos Sci*, 21, 662-674, <https://doi.org/10.1007/BF02915733>,  
494 2004.
- 495 Xia, S. W., Yin, Z. C., and Wang, H. J.: Remote Impacts from Tropical Indian Ocean on January Haze Pollution  
496 over the Yangtze River Delta, *Atmos Ocean Sci Lett*, 14, 100042, <https://doi.org/10.1016/j.aosl.2021.100042>,  
497 2021.
- 498 Xu, H. W., Chen, H. P., and Wang, H. J.: Interannual variation in summer extreme precipitation over Southwestern  
499 China and the possible associated mechanisms, *Int J Climatol.* 41, 3425–3438, <https://doi.org/10.1002/joc.7027>,  
500 2021.
- 501 Xu, W. Y., Xu, X. B., Lin, M. Y., Lin, W. L., Tarasick, D., Tang, J., Ma, J. Z., and Zheng, X. D.: Long-term trends  
502 of surface ozone and its influencing factors at the Mt Waliguan GAW station, China – Part 2: The roles of  
503 anthropogenic emissions and climate variability, *Atmos. Chem. Phys.*, 18, 773–798, [https://doi.org/10.5194/acp-](https://doi.org/10.5194/acp-18-773-2018)  
504 [18-773-2018](https://doi.org/10.5194/acp-18-773-2018), 2018.
- 505 Yang, Y., Liao, H., and Li, J.: Impacts of the East Asian summer monsoon on interannual variations of summertime  
506 surface-layer ozone concentrations over China, *Atmos. Chem. Phys.*, 14, 6867–6879, [https://doi.org/10.5194/acp-](https://doi.org/10.5194/acp-14-6867-2014)  
507 [14-6867-2014](https://doi.org/10.5194/acp-14-6867-2014), 2014.
- 508 Yin, Z. C., and Ma, X. Q.: Meteorological Conditions Contributed to Changes in Dominant Patterns of Summer  
509 Ozone Pollution in Eastern China, *Environ. Res. Lett.*, 15, 124062, <https://doi.org/10.1088/1748-9326/abc915>,  
510 2020.
- 511 Yin, Z. C., Wang, H. J., Li, Y. Y., Ma, X. H., and Zhang, X. Y.: Links of Climate Variability among Arctic sea ice,  
512 Eurasia teleconnection pattern and summer surface ozone pollution in North China, *Atmos. Chem. Phys.*, 19,  
513 3857–3871, <https://doi.org/10.5194/acp-19-3857-2019>, 2019.
- 514 Zhao, Z. J., and Wang, Y. X.: Influence of the west pacific subtropical high on surface ozone daily variability in  
515 summertime over eastern China, *Atmos. Environ.*, 170, 197–204, <https://doi.org/10.1016/j.atmosenv.2017.09.024>,  
516 2017.
- 517 Zhou, D. R., Ding, A. J., Mao, H. T., Fu, C. B., Wang, T., Chan, L. Y., Ding, K., Zhang, Y., Liu, J., Lu, A., and  
518 Hao, N.: Impacts of the East Asian monsoon on lower tropospheric ozone over coastal South China, *Environ. Res.*  
519 *Lett.*, 8, 044011, <https://doi.org/10.1088/1748-9326/8/4/044011>, 2013.



520 **Table and Figure captions**

521 **Figure 1.** (a) Spatial distributions of observed (dots) and GEOS-Chem simulated (shading) summer-mean MDA8  
522 O<sub>3</sub> (unit:  $\mu\text{g m}^{-3}$ ) for the period 2015–2019. (b) The second EOF spatial pattern of simulated summer-mean MDA8  
523 O<sub>3</sub> from 1980 to 2019. The simulated O<sub>3</sub> concentrations were produced by GEOS-Chem with fixed emissions but  
524 changing meteorological conditions from 1980 to 2019. The green boxes represent the areas of NC and the PRD.

525 **Figure 2.** Variations in standardized DP-O<sub>3</sub> time series (black), SI<sub>FJL</sub> (red), SIOD (blue), and SEI (green) from  
526 1980 to 2019. The correlation coefficients of the DP-O<sub>3</sub> with SI<sub>FJL</sub> (red), SIOD (blue), and SEI (green) were shown  
527 in the figure.

528 **Figure 3.** Composite summer atmospheric circulations associated with the DP-O<sub>3</sub> (DP-O<sub>3</sub>P minus DP-O<sub>3</sub>N) for  
529 the period 1980 to 2019, including (a) SAT (unit: K, shadings) and geopotential height at 500 hPa (unit: gpm,  
530 contours), (b) Ssr (unit:  $10^6 \text{ J m}^{-2}$ , shadings) and Mlcc (unit: 1, contours), and (c) Prec (unit: mm, shadings) and  
531 surface wind (unit:  $\text{m s}^{-1}$ , arrows). The white dots indicate that the composites with shading were above the 90%  
532 confidence level. The black boxes in (a) indicate the centers of the AC<sub>NC</sub> and C<sub>PRD</sub>, respectively. The green boxes  
533 in (b) and (c) represent the areas of NC and the PRD.

534 **Figure 4.** Composites of (a) May SI concentration and (b) JFM SST associated with the DP-O<sub>3</sub> (DP-O<sub>3</sub>P minus  
535 DP-O<sub>3</sub>N) from 1980 to 2019. The green boxes in (a) and (b) indicate where the SI<sub>FJL</sub> and SIOD indices are  
536 calculated, respectively. The white dots indicate that the composites were above the 90% confidence level.  
537 Composite summer meteorological conditions and circulations associated with (c) SI<sub>FJL</sub> (positive SI<sub>FJL</sub> years minus  
538 negative SI<sub>FJL</sub> years) and (d) SIOD (positive SIOD years minus negative SIOD years) from 1980 to 2019,  
539 including the differences in Ssr (unit:  $10^6 \text{ J m}^{-2}$ ), SAT (unit: K), and Prec (unit: mm) between NC and the PRD  
540 (NC minus PRD), and the differences between AC<sub>NC</sub> and C<sub>PRD</sub>. The black slashes indicate that the composites  
541 were above the 90% confidence level.

542 **Figure 5.** Composites of (a) May Arctic SST (unit: K) and (c) Rossby wave source anomalies at 500 hPa (unit:  
543  $10^{-11} \text{ s}^{-2}$ ) associated with SI<sub>FJL</sub> index (negative SI<sub>FJL</sub> years minus positive SI<sub>FJL</sub> years) from 1980 to 2019. (b, d)  
544 same as (a, c) but for JJA. The shadings, contours and vectors in (c, d) represent Rossby wave source, velocity  
545 potential (unit:  $10^5 \text{ m}^2 \text{ s}^{-1}$ ) and divergent wind (unit:  $\text{m s}^{-1}$ ), respectively. The yellow box in (c) and green box in  
546 (d) represents the center of the velocity potential and Rossby wave source anomaly associated with SI<sub>FJL</sub>,  
547 respectively. The white dots indicate that the composites with shading were above the 90% confidence level.

548 **Figure 6.** Composites of (a) wave activity flux anomalies (unit:  $\text{m}^2 \text{ s}^{-2}$ , arrows), geopotential height (unit: gpm,  
549 shading) at 500 hPa and (b) mean wind (unit:  $\text{m s}^{-1}$ , arrows), omega (unit:  $10^{-2} \text{ Pa s}^{-1}$ , shading) over 100–130° E,  
550 and the anomalies of AC<sub>NC</sub> and C<sub>PRD</sub> (unit: gpm, bar) in summer associated with SI<sub>FJL</sub> index (negative SI<sub>FJL</sub> years  
551 minus positive SI<sub>FJL</sub> years) from 1980 to 2019. The green boxes in (a) represent the centers of the EU-like pattern.  
552 The white dots indicate that the composites with shading were above the 90% confidence level.

553 **Figure 7.** Composite differences of geopotential height at 500 hPa in JJA between three low and high SI<sub>FJL</sub> years  
554 based on the ensemble of 40 CESM-LE simulations during 1980–2019. The black dots indicate that the  
555 mathematical sign of the composite results of more than 60 % of the members is consistent with the ensemble  
556 mean. The black boxes represent the centers of the EU-like pattern.



557 **Figure 8.** (a) Composites of mean 0–60m subsurface ocean temperature (unit: K) in summer associated with the  
558 SIOD (positive SIOD years minus negative SIOD years) from 1980 to 2019. The green boxes represent the centers  
559 of the SIOD, and the black box indicates where the SOT index is calculated. Composites of (b) OLR (unit:  $W m^{-2}$ )  
560 and (c) velocity potential (unit:  $10^5 m^2 s^{-1}$ , shadings) and divergent winds (unit:  $m s^{-1}$ , vectors) at 1000 hPa in  
561 summer associated with SOT indexes of opposite sign (negative SOT years minus positive SOT years). The black  
562 box represents the center of the SOT. (d) Composites of summer mean winds (unit:  $m s^{-1}$ , arrows) and omega (unit:  
563  $10^{-2} Pa s^{-1}$ , shadings) over 90–120°E, and the anomalies of  $AC_{NC}$  and  $C_{PRD}$  (unit: gpm, bars) associated with SOT  
564 indexes of opposite sign. The white dots indicate that the composites with shading were above the 90% confidence  
565 level.

566 **Figure 9.** Composite differences of geopotential height at 500 hPa in JJA between three high and low SIOD years  
567 based on the ensemble of 40 CESM-LE simulations during 1980–2019. The black dots indicate that the  
568 mathematical sign of the composite results of more than 60 % of the members is consistent with the ensemble  
569 mean. The black boxes represent the centers of  $AC_{NC}$  and  $C_{PRD}$ , respectively.

570 **Figure 10.** Schematic diagrams of the associated physical mechanisms. The May SI anomalies near the Franz  
571 Josef Land (red shadings) could trigger an EU-like pattern in the atmosphere in summer, which enhances the  
572 anticyclonic anomaly over NC and the cyclonic anomaly over the PRD. The thermodynamic signal of the  
573 preceding SIOD (contours) could be stored in the subsurface and the center of negative SST anomalies moves to  
574 the vicinity of Sumatra Island in summer (blue shading). The meridional circulation was enhanced in summer  
575 (dashed lines), along with the enhancement of  $AC_{NC}$  and  $C_{PRD}$  over eastern China. The solid lines indicate the  
576 anomalous atmospheric circulations affected by  $SI_{FJL}$ , while the dashed lines indicate the anomalous atmospheric  
577 circulations affected by SIOD.

578 **Figure 11.** (a) Composites of geopotential height at 500 hPa (unit: gpm, shadings) in summer associated with the  
579 SEI (positive SEI years minus negative SEI years) from 1980 to 2019. The red and blue lines indicate areas where  
580 the composite geopotential height anomalies associated with  $SI_{FJL}$  and SIOD exceed the 90% confidence level,  
581 respectively. The black boxes represent the centers of  $AC_{NC}$  and  $C_{PRD}$ , respectively. (b) Composite differences of  
582 the detrended summer-mean MDA8  $O_3$  (unit:  $\mu g m^{-3}$ ) simulated by GEOS-Chem model between high and low  
583 SEI years during 1980–2019. The white dots indicate that the composite differences are above the 90% confidence  
584 level. The green boxes represent the areas of NC and the PRD.

585

586